Phase-dependent microwave response of a graphene Josephson junction

R. Haller [1,*] G. Fülöp [1,2] D. Indolese,[1] J. Ridderbos [1] R. Kraft,[3,4] L. Y. Cheung,[1] J. H. Ungerer,[1,5] K. Watanabe [6]
T. Taniguchi [7] D. Beckmann [8] R. Danneau [8] P. Virtanen [9] and C. Schönenberger [1,5,†]

[1]*Department of Physics, University of Basel, Klingelbergstrasse 82 CH-4056, Switzerland*
[2]*Department of Physics, Budapest University of Technology and Economics and*
MTA-BME Momentum Nanoelectronics Research Group, H-1111 Budapest, Budafoki út 8, Hungary
[3]*Institute of Nanotechnology, Karlsruhe Institute of Technology, D-76021 Karlsruhe, Germany*
[4]*Institute of Physics, Karlsruhe Institute of Technology, D-76131 Karlsruhe, Germany*
[5]*Swiss Nanoscience Institute, University of Basel, Klingelbergstrasse 82 CH-4056, Switzerland*
[6]*Research Center for Functional Materials, National Institute for Materials Science, 1-1 Namiki, Tsukuba 305-0044, Japan*
[7]*International Center for Materials Nanoarchitectonics, National Institute for Materials Science, 1-1 Namiki, Tsukuba 305-0044, Japan*
[8]*Institute of Quantum Materials and Technologies, Karlsruhe Institute of Technology, D-76021 Karlsruhe, Germany*
[9]*Department of Physics and Nanoscience Center, University of Jyväskylä, P.O. Box 35 (YFL), University of Jyväskylä FI-40014, Finland*

Gate-tunable Josephson junctions embedded in a microwave environment provide a promising platform to *in situ* engineer and optimize novel superconducting quantum circuits. The key quantity for the circuit design is the phase-dependent complex admittance of the junction, which can be probed by sensing a radio frequency SQUID with a tank circuit. Here, we investigate a graphene-based Josephson junction as a prototype gate-tunable element enclosed in a SQUID loop that is inductively coupled to a superconducting resonator operating at 3 GHz. With a concise circuit model that describes the dispersive and dissipative response of the coupled system, we extract the phase-dependent junction admittance corrected for self-screening of the SQUID loop. We decompose the admittance into the current-phase relation and the phase-dependent loss, and as these quantities are dictated by the spectrum and population dynamics of the supercurrent-carrying Andreev bound states, we gain insight to the underlying microscopic transport mechanisms in the junction. We theoretically reproduce the experimental results by considering a short, diffusive junction model that takes into account the interaction between the Andreev spectrum and the electromagnetic environment, from which we estimate lifetimes on the order of $\sim$10 ps for nonequilibrium populations.

I. INTRODUCTION

For Josephson junctions (JJs), in which the superconducting electrodes are linked with a short normal-conducting region, the coherent superconducting interaction is promoted by so-called Andreev bound states (ABSs) [1]. The material and geometrical properties of the weak link together with the superconducting phase difference φ across the JJ define the energy of the ABSs [2]. Their structure and occupation dynamics determine the inductive and dissipative microwave response, i.e., the admittance of the JJ [3,4]. In particular, the inductive response relates to the time-averaged dispersion of the populated ABSs and reflects the phase dependence of the supercurrent $I_s(\varphi)$ across the junction [5,6], which is known as the current-phase relation (CPR). However, the dissipative response relates to the fluctuations in the ABS population

resulting in temporal changes of the supercurrent [7,8]. The microscopic source for those dynamics are thermally activated or microwave induced short-lived ABS excitations [9]. Conclusively, the junction admittance, which is the key quantity to engineer high-frequency Josephson circuits, is highly dependent on the underlying microscopic processes.

The junction admittance can be probed as a function of phase by embedding a JJ in an radio frequency (rf) SQUID that couples to a resonator [9–13]. The rf SQUID acts as a magnetic flux-tunable complex impedance in the circuit that shifts and broadens the resonate behavior, from which one can infer the phase-dependent inductive and dissipative response of the junction [14]. The strong demand for *in situ* controllable junctions in microwave applications has raised the attention to JJs consisting of gate-tunable weak links [15]. Here, we determine the full complex admittance of a Josephson weak link made of graphene, which is a two-dimensional (2D) material with a linear band structure and excellent gating properties.

Although graphene JJs have already demonstrated their compatibility in different superconducting high-frequency circuits, such as bolometers [16,17], transmon qubits [18,19], and tunable microwave cavities [20], only few experiments have addressed the determination of their phase-dependent
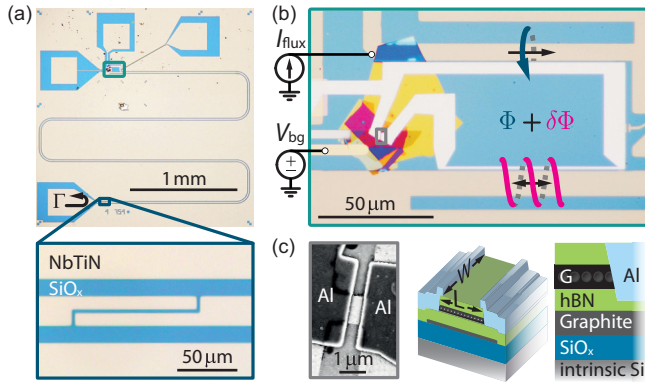

FIG. 1. Graphene rf SQUID inductively coupled to a superconducting transmission line resonator. (a) Optical image of the NbTiN $\lambda/4$-resonator consisting of a meandered coplanar transmission line with the shorted end (current anti-node) on top, seen also at the bottom of image (b), and the open end (current node) at the bottom, shown in the zoom-in. (b) Optical image of the monolayer graphene (G) Josephson junction (JJ) embedded in an Al loop forming the rf SQUID. The DC current I_{flux} creates a flux Φ inside the loop (blue line), which allows to phase bias the junction. The inductive coupling to the resonator induces a small oscillating probe flux $\delta\Phi$ (red lines). The gate voltage V_{bg} applied on the bottom graphite sheet tunes the charge carrier density in G. (c) Scanning electron micrograph and cross-sectional schematics of the hBN-encapsulated G-JJ with Al side-contacts of width $W = 1\,\mu$m and length $L = 400$ nm.

admittance [13,21]. While Ref. [13] has been focusing on the phase-dependent dissipation of the junction under the influence of external irradiation and Ref. [21] on the inductive behavior, we here investigate both the inductive and dissipative response simultaneously by studying the inherent photonic phase-dependent interplay between the sensing resonator and the graphene JJ. We present a classical, comprehensive circuit model to infer the full complex junction admittance from the reflective response of a graphene rf SQUID coupled to a superconducting microwave resonator operating at $\sim$3 GHz. We further translate this to the CPR and the phase-dependent dissipation as a function of gate voltage, under consideration of the self-screening effect that arises due to the finite inductance of the SQUID loop. We describe our observations within the framework of ABSs and find remarkable agreement between the experimental results and the theoretically predicted microwave response of a short, diffusive junction.

II. DEVICE

The device is presented in Fig. 1 and consists of a graphene JJ embedded in a superconducting loop, which inductively couples to a coplanar transmission line (CTL) resonator. The resonant structure and supply lines are etched into NbTiN (80 nm) sputtered on an intrinsic Si/SiO$_x$ (500 μm/170 nm) substrate. The meandered CTL shown in Fig. 1(a) is shorted to ground on one side, and interrupted by a coupling capacitor on the other. Both of these terminations act as microwave mirrors of the opposite type, and thereby form a superconducting $\lambda/4$-resonator with a fundamental bare resonance frequency $f_{\text{bare}} = 3.098$ GHz.

The graphene JJ, shown in Fig. 1(c), is made of a van der Waals heterostructure consisting of a monolayer graphene encapsulated in hexagonal boron nitride (hBN). The lower hBN layer (47.5 nm) separates the graphene flake from the bottom graphite gate. A thermally evaporated Ti/Al (5 nm/90 nm) lead contacts the graphene from both sides [22] and encloses the junction in a loop, thus forming a graphene rf SQUID, which is inductively coupled to the current anti-node of the resonator as illustrated in Fig. 1(b). The galvanic grounding of the loop defines the reference potential for the gate voltage V_{bg} applied on the bottom graphite structure. The DC current I_{flux} controls the magnetic flux Φ inside the loop and therefore tunes the external phase difference $\varphi_{\text{ext}} = 2\pi\Phi/\Phi_0$ across the rf SQUID, where $\Phi_0 = h/2e$ is the superconducting flux quantum with h being the Planck constant and e the elementary charge. Consider the Supplemental Material (SM) for details about the device fabrication [23].

In the subsequent experiment we perform reflectance measurements on the port denoted by Γ in Fig. 1(a) and investigate the resonant circuit as a function of V_{bg} and I_{flux}, from which we later infer the CPR and the phase-dependent loss of the graphene JJ.

III. REFLECTOMERTY

The coupled microwave circuit is probed by reflectometry in a dry dilution refrigerator, in which the device is surrounded by a permalloy shield. With a vector network analyzer we measure the complex reflection coefficient Γ as a function of probe frequency f and I_{flux}. We ensure a quasiequilibrium sensing by setting the probe power to an averaged intracavity occupation of $\sim$100 photons, which corresponds to an oscillating probe flux $\delta\Phi \approx \Phi_0/100$ inside the SQUID loop. Additionally, we tune the charge carrier density in the graphene layer by applying a gate voltage in the range $V_{\text{bg}} = [-9, 9]$ V. The conversion from V_{bg} to charge carrier density as well as the measurement scheme and the calibration of the probe power can be found in the SM [23].

The reflective response at $V_{\text{bg}} = 6$ V presented in Fig. 2 is exemplary for the whole measurement set. Clear periodic shifts of the resonance frequency f_0 as a function of I_{flux} can be observed in Figs. 2(a) and 2(b). We encounter no phase jumps and relate the external phase $\varphi_{\text{ext}} = n_{\text{odd}}\pi$ $(= n_{\text{even}}\pi)$ to points of minimal (maximal) resonance frequencies [10,14]. Besides f_0, the resonance lineshape also changes as seen in Figs. 2(c) and 2(d) when comparing line cuts at $\varphi_{\text{ext}} = -\pi$ and $\varphi_{\text{ext}} = 0$. As we will show, both the modulation in f_0 and the altered lineshape are the consequence of the phase-dependent complex admittance of the graphene JJ.

To characterize the JJ from the reflective response, we fit $|\Gamma|$ and $\arg(\Gamma)$ simultaneously for each combination of V_{bg} and I_{flux} with the complex resonance curve of a loaded $\lambda/4$-resonator expressed according to Ref. [24] as

$$\Gamma = \left[\frac{\Gamma_{\text{min}} + 2jQ\frac{f-f_0}{f_0}}{1 + 2jQ\frac{f-f_0}{f_0}} - 1\right]e^{j\phi} + 1. \quad (1)$$

Thus, we can deduce f_0 and assess the broadening of the resonance curve. The latter is determined by the total quality factor $Q = 1/(Q_{\text{load}}^{-1} + Q_i^{-1} + Q_c^{-1})$, which in turn, consists
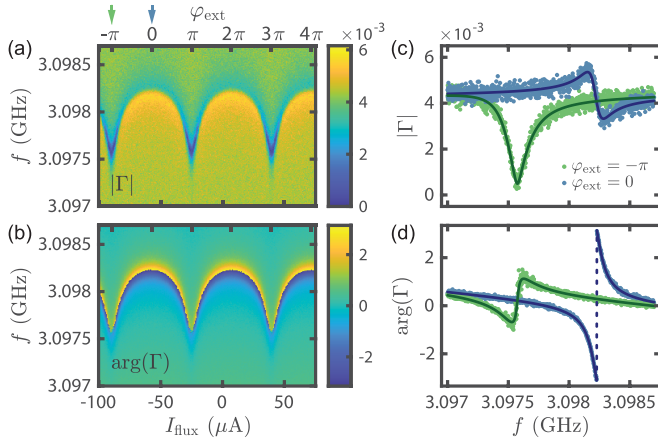
FIG. 2. Flux dependence of the reflection coefficient Γ at $V_{bg} = 6$ V. (a, b) Colormaps of $|\Gamma|$ and $\arg(\Gamma)$ as a function of probe frequency f and DC flux current I_{flux}. The horizontal top axis represents the conversion to the external phase φ_{ext} across the rf SQUID. (c, d) $|\Gamma|$ and $\arg(\Gamma)$ at $\varphi_{ext} = [-\pi, 0]$ overlaid with fits to Eq. (1) (solid lines), from which we obtain the resonance frequency f_0, asymmetry angle ϕ, coupling quality factor Q_c and effective quality factor Q_e as listed below:

φ_{ext}	f_0	ϕ	Q_c	Q_e
$-\pi$	3.09755 GHz	0.224	23 400	19 400
0	3.09821 GHz	0.235	23 700	>200 000

of three different dissipation sources: (i) The inverse load quality factor Q_{load}^{-1} describes loss generated by the rf SQUID, (ii) the inverse internal quality factor Q_i^{-1} describes loss inherent to the properties of the CTL, and (iii) the inverse coupling quality factor Q_c^{-1} describes loss to the measurement environment. Here, Q_{load}^{-1} and Q_i^{-1} are merged to an effective quality factor $Q_e = 1/(Q_{load}^{-1} + Q_i^{-1})$. Furthermore, we define $\Gamma_{min} = (Q_c - Q_e)/(Q_c + Q_e)$ and introduce the angle ϕ, which accounts for an asymmetric line shape.

The fits to Eq. (1) at $\varphi_{ext} = -\pi$ and $\varphi_{ext} = 0$, shown in Figs. 2(c) and 2(d) as solid lines, reveal an overall shift of 660 kHz in f_0 and a drastic change in Q_e, while Q_c and ϕ remain similar. At $\varphi_{ext} = -\pi$, we obtain $Q_e = 19\,400$ and $Q_c = 23\,400$, whereas at $\varphi_{ext} = 0$, we find $Q_e > 200\,000$ and $Q_c = 23\,700$. Consequently, the resonator is undercoupled ($Q_e < Q_c$) at $\varphi_{ext} = -\pi$, but overcoupled ($Q_e > Q_c$) at $\varphi_{ext} = 0$, which explains the distinct resonance lineshapes [25]. Since Q_i can be treated as a constant with Q_e being a lower bound, we conclude that $Q_i > 200\,000$. This large value allows us to treat the CTL as lossless ($Q_i^{-1} = 0$) such that $Q_e \approx Q_{load}$. The SM provides further insights to the resonance curve fitting [23].

The observed flux tunable microwave response in terms of f_0 and Q_{load} is the direct manifestation of phase-dependent microscopic processes in the graphene JJ [10], which will be discussed in detail in Secs. VII and VIII within the framework of ABSs. In the following section we model the electrical properties of the graphene JJ with lumped elements and explain their effect on the resonant behavior with the circuit of a loaded $\lambda/4$-resonator.
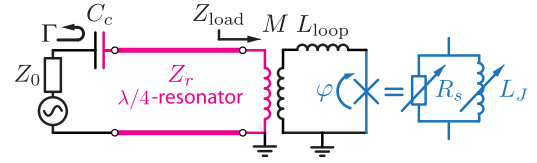

FIG. 3. Circuit schematic of a rf SQUID coupled to a $\lambda/4$ resonator. The resonator couples inductively to the rf SQUID with strength M and connects to the reflectometry setup via capacitance C_c. The rf SQUID is modeled as a loop with self-inductance L_{loop} in series with the JJ, which in turn, is modeled as a variable Josephson inductance L_J in parallel with a variable shunt resistance R_s. This forms a variable load impedance Z_{load}, which tunes the reflective response Γ.

IV. CIRCUIT MODEL

The inductively coupled rf SQUID acts as a variable load impedance Z_{load} attached to the resonator, which tunes the reflective response. We express Z_{load} according to the circuit schematic depicted in Fig. 3. The rf SQUID is modeled as a loop with self-inductance L_{loop} in series with the JJ. The mutual inductance M quantifies the coupling strength to the resonator, which is built from a CTL with characteristic impedance Z_r. The JJ itself is represented by a variable Josephson inductance L_J in parallel with a variable shunt resistance R_s. For this arrangement the load impedance terminating the resonator is detailed in the SM and reads [23]

$$Z_{load} = \frac{\omega^2 M^2}{j\omega L_{loop} + (G_s + jB_J)^{-1}}, \qquad (2)$$

where $\omega = 2\pi f$ is the angular frequency, $G_s = 1/R_s$ is the shunt conductance and $B_J = -1/(\omega L_J)$ is the susceptance. Note that $Y = G_s + jB_J$ is the complex admittance of the JJ.

The influence of Z_{load} on the $\lambda/4$-resonator is twofold: First, the imaginary part of Z_{load} causes a shift of the resonance frequency as derived in the SM [23],

$$\delta f_0 = f_0 - f_{bare} = -\frac{2}{\pi Z_r} \text{Im}(Z_{load}) f_{bare}, \qquad (3)$$

with respect to the unloaded resonance frequency f_{bare}. Second, the real part of Z_{load} gives rise to dissipation in the resonant circuit, which can be expressed according to the derivations presented in the SM as [23]

$$Q_{load} = \frac{\pi Z_r}{4 \, \text{Re}(Z_{load})}. \qquad (4)$$

From Eq. (2) one recognizes that the junction variables, G_s and B_J affect both $\text{Re}(Z_{load})$ and $\text{Im}(Z_{load})$. Consequently, δf_0 and Q_{load} would need to be considered simultaneously to evaluate them. However, it turns out that, due to the obtained relatively large Q_{load} values, one is allowed to set $G_s \to 0$ in Eq. (3), which simplifies the relation as shown in the SM to [23]

$$\delta f_0 \approx \frac{8}{\pi^2} \frac{M^2}{L_p(L_J + L_{loop})} f_{bare}, \qquad (5)$$

where L_p is the parallel LC-equivalent inductance of the $\lambda/4$-resonator. This means that the shift of the resonance
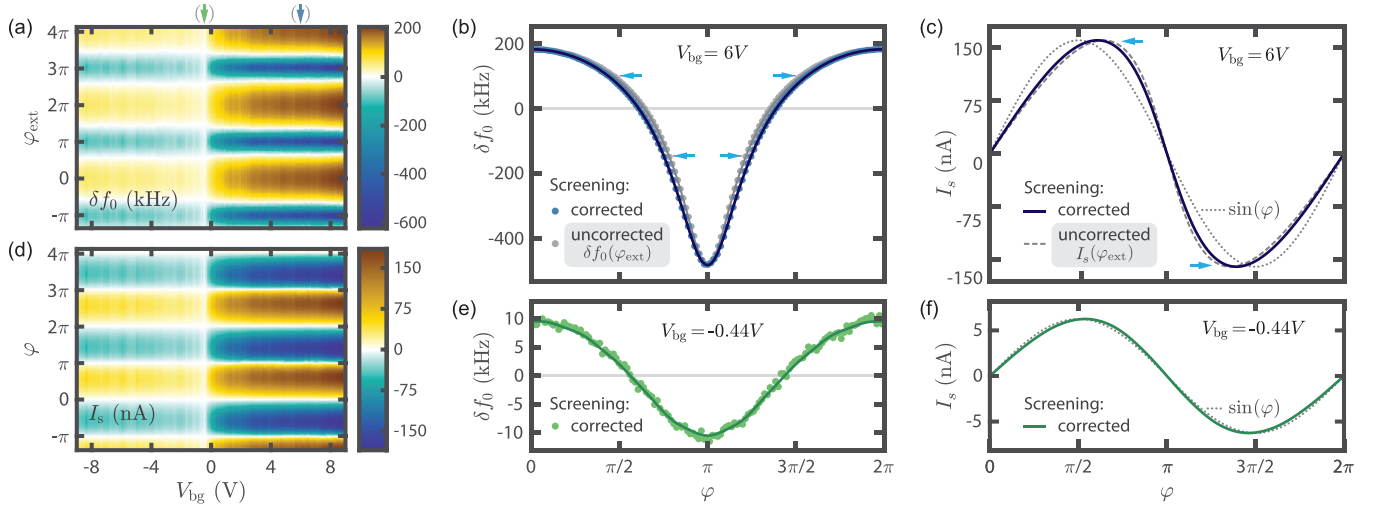
FIG. 4. Evaluation of the CPR. (a) Colormap of the resonance frequency shift $\delta f_0 = f_0 - f_{\mathrm{bare}}$ with $f_{\mathrm{bare}} = 3.098$ GHz as a function of gate voltage V_{bg} and external phase φ_{ext}. (b) δf_0 at $V_{\mathrm{bg}} = 6$ V as a function of φ and φ_{ext}, respectively overlaid with the fits to Eq. (5) (solid lines), from which the CPR is deduced. (c) Presents the CPR at $V_{\mathrm{bg}} = 6$ V, corrected for the self-screening of the SQUID (blue) and uncorrected (dashed), in comparison with the sine function (dotted). In panels (b, c) arrows illustrate the correction introduced by the nonlinear mapping from φ_{ext} to φ. (d) Corrected CPR inferred from panel (a) as a function of V_{bg}. (e) δf_0 at the charge neutrality point ($V_{\mathrm{bg}} = -0.44$ V) as a function of φ overlaid with the fit and in panel (f) the corresponding CPR.

frequency mainly originates from the Josephson inductance L_J, whereas the broadening of the resonance originates from the dissipation in the JJ specified by the shunt conductance G_s.

Since the inverse Josephson inductance is a measure of the change in the supercurrent $I_s(\varphi)$ with respect to the phase φ across the junction [6],

$$L_J(\varphi)^{-1} = \frac{2\pi}{\Phi_0} \frac{\partial I_s(\varphi)}{\partial \varphi}, \qquad (6)$$

we can express the resonance frequency shift and the behavior of $L_J(\varphi)$ with the current-phase relation (CPR).

To quantify the CPR and G_s from the resonator response, we perform finite-element simulations [26] based on the device geometry, to acquire $L_{\mathrm{loop}} = 211$ pH and $M = 30.83$ pH. Moreover, we find $Z_r = 69.5\,\Omega$ from the aspect ratios of the CTL [27] in combination with the resonant behavior of the circuit and deduce $L_p = 4.55$ nH. The evaluation of Z_r and L_p can be found in the SM [23].

V. CURRENT-PHASE RELATION

In this section we extract the CPR by fitting the periodic shift of the resonance frequency under consideration of self-screening effects. The coupling strength between the superconducting leads is determined by the Cooper pair transmission probability and defines the shape of the CPR. For small coupling or low transmission probability the CPR is sinusoidal, whereas the CPR becomes forward-skewed for increased coupling. Due to the semiconducting properties in graphene JJs, the coupling strength and therefore the CPR skewness can be tuned with the gate voltage [20,28–31]. To capture the nonsinusoidal behavior, we express the CPR as Fourier series [32]

$$I_s(\varphi) = \sum_k (-1)^{k-1} A_k \sin(k\varphi), \qquad (7)$$

with k being the harmonic order and A_k the corresponding amplitude.

To extract the CPR from the measured resonance frequency modulations, we need to relate the external phase φ_{ext} to the phase difference φ across the JJ. This is not straightforward, since if a supercurrent flows within the rf SQUID, there is a phase drop over the loop inductance L_{loop} in addition to the phase drop over the JJ, which leads to a nonlinear relation between the internal phase φ and the external phase φ_{ext}— known as the screening effect [33]:

$$\varphi = \varphi_{\mathrm{ext}} - \frac{2\pi}{\Phi_0} L_{\mathrm{loop}} I_s(\varphi). \qquad (8)$$

Here, we obtain the CPR for each gate voltage by solving the set of equations Eqs. (5)–(8) in a self-consistent way by using an iterative fitting method. The basis for this method is the resonance frequency shift as a function of φ_{ext}, which is presented for the entire gate range in Fig. 4(a). At each fitting iteration we include Fourier amplitudes A_k up to the 10th-harmonic and allow for small changes in f_{bare}. Details about the method can be found in the SM [23].

In Fig. 4(b) we illustrate the effect of screening by comparing δf_0 as a function of φ and φ_{ext}, respectively—for the example at $V_{\mathrm{bg}} = 6$ V. The corresponding CPRs, deduced from fitting the modulations in δf_0 with respect to phase, shown as solid lines in Fig. 4(b), are presented in Fig. 4(c). The screening consideration causes a distortion of the phase around π as indicated by arrows. Omitting this effect results in an apparent enhancement of the skewness [34]. Even after correcting for screening, we find a substantially forward-skewed CPR, visualized by the comparison with a sinusoidal behavior. Although screening effects are small in this case, we emphasize that they can have a significant impact on the evaluated skewness, especially for large I_s and L_{loop}.

In Fig. 4(d) we map the extracted CPR as a function of V_{bg}. The smallest CPR amplitude is found at $V_{\mathrm{bg}} = -0.44$ V,
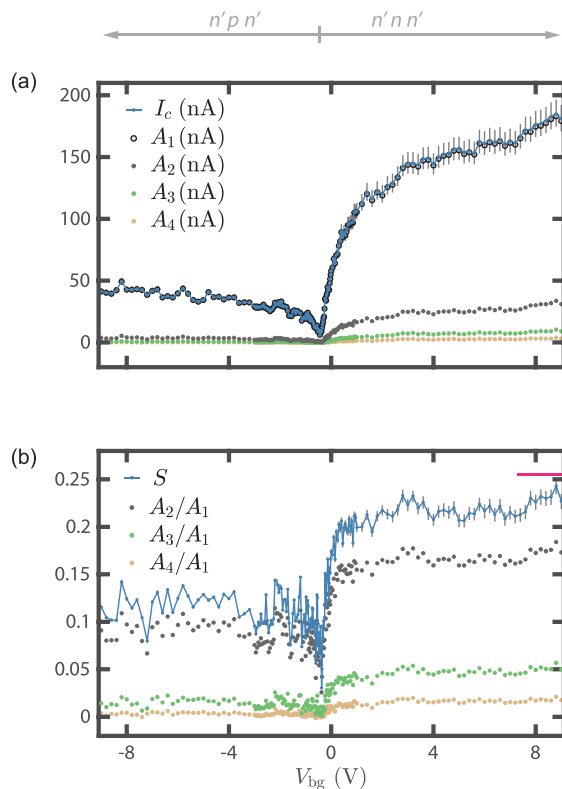
FIG. 5. Characteristics of the CPR as function of gate voltage V_{bg}. The step size in V_{bg} is reduced close to the CNP ($V_{bg} = -0.44$ V). (a) Critical current I_c and Fourier amplitudes A_k. (b) Skewness parameter S and ratios A_k/A_1. The theoretical skewness value for a short, diffusive system under ideal conditions $S = 0.255$ is illustrated with the pink mark. (a, b) Systematic error bars in I_c and S are generated by modifying M by $\pm 3\%$ and L_{loop} by $\pm 5\%$ in the CPR evaluation. The amplitudes A_k for $k \geqslant 5$ are negligibly small and omitted in the figures.

FIG. 6. Evaluation of the shunt conductance G_s. (a) The load quality factor Q_{load} in logarithmic scale as a function of V_{bg} and φ, deduced from resonance curve fittings. (b) G_s in logarithmic scale obtained by using Eq. (4) with Q_{load} and the CPR results. (c) Phase dependence of G_s for different gate voltages. (d) Gate dependence of G_s for phase biasing conditions $\varphi = n_{odd}\pi$. These correspond to the local dissipation maxima, indicated by the horizontal arrows in panel (b).

which we attribute to the charge neutrality point (CNP) of graphene. Here, resonance frequency modulations of only ± 10 kHz can still be clearly resolved as seen in Fig. 4(e), which demonstrates the sensitivity of the microwave circuit. The CPR at the CNP, shown in Fig. 4(f), is slightly skewed and has a maximal supercurrent of $I_c = 6.3$ nA.

In the following, we quantify the CPR and its skewness by two commonly used ways: (i) by the skewness parameter $S = (2\varphi_{max}/\pi) - 1$, where φ_{max} is the phase maximizing the CPR to the critical current I_c [29], and (ii) by directly providing the set of Fourier amplitudes A_k [32]. The latter description is more precise, since it captures the entire CPR lineshape, whereas the S-parameter together with I_c do not uniquely characterize the CPR, but are more intuitive.

In Fig. 5 we employ both of these characterizations to illustrate the gate dependence of the CPR. We observe a rapid enhancement of I_c up to ~200 nA for gating toward positive voltages (n-doped), whereas toward negative voltages (p-doped) the increase is weaker and reaches only ~50 nA as seen in Fig. 5(a). Because A_1 closely follows I_c, the CPR is mainly determined by the 2π-periodic sinusoidal contribution for all V_{bg}. However, the small additions from higher harmonics lead to a forward-skewed CPR. From Fig. 5(b) it
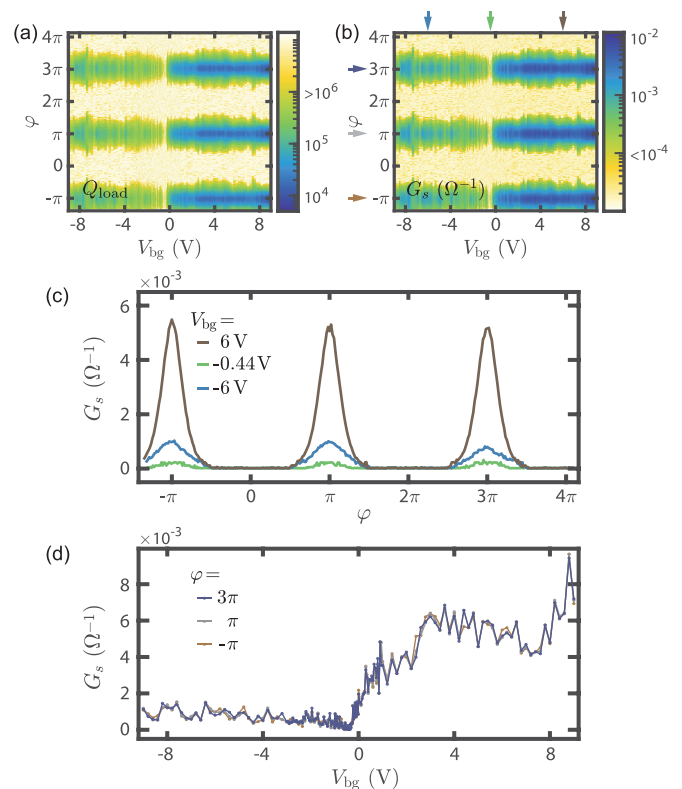
appears that the skewness saturates in both doping regimes with a slight reduction around the CNP. For the n-doped side, the skewness saturates around $S \approx 0.22$, whereas on the p-doped side the skewness is less pronounced, saturating around $S \approx 0.12$. The ratios A_k/A_1 follow the same trend.

The asymmetric behavior in I_c and S with respect to V_{bg} are attributed to the presence of n'-doped contact regions inducing additional scattering potentials. The JJ is therefore more transparent in the $n'nn'$ situation compared to the $n'pn'$ case [29,35]. We speculate that the minimal skewness of $S \approx 0.05$ close to the CNP originates from the formation of electron-hole puddles [36] in the graphene flake, which further enhance the scattering probability.

VI. PHASE-DEPENDENT LOSS

Having extracted the CPR from the resonance frequency shift, we now deduce the phase-dependent dissipative part of the graphene JJ; namely, the shunt conductance G_s. We can infer G_s from Eq. (4), in which we express the susceptance B_J with the CPR according to Eq. (6) and make use of Q_{load} obtained from the reflectance curve analysis presented in Sec. III.

From Fig. 6(a), we observe that around the 0-points ($\varphi = n_{\mathrm{even}}\pi$) the dissipation in the microwave circuit stemming from the rf SQUID is minor ($Q_{\mathrm{load}} > 200\,000$) for all V_{bg}. However, at the π-points ($\varphi = n_{\mathrm{odd}}\pi$), the dissipation becomes significantly larger and gate dependent with a minimal quality factor of $Q_{\mathrm{load}} \approx 9800$.

This behavior is reflected in G_s, which is mapped in Fig. 6(b) as a function of V_{bg} and φ. Around the 0-points, we deduce low conductance values $G_s \leqslant 0.1 \text{ m}\Omega^{-1}$, which refers to weak dissipation according to the parallel junction circuit model used here. In contrast, at the π-points, a pronounced Lorentzian-shaped dissipation peak develops, as seen in Fig. 6(c). The dissipation onsets are located symmetrically around the π-points and are weakly gate dependent. However, the peak heights are strongly influenced by V_{bg} and reach a maximal value of $G_s \approx 10 \text{ m}\Omega^{-1}$ at large n-doping. Although the amplitude of the peak appears to fluctuate as a function of V_{bg}, the height replicates for the three different π-points measured here, as illustrated in Fig. 6(d). This demonstrates the stability of the gate-tunable potential landscape in graphene. To explain the dissipative response of the JJ, the underlying phase-dependent transport processes need to be consider, which are discussed in the next section.

VII. THEORY OF ANDREEV BOUND STATES

In the following we relate the CPR and the phase-dependent dissipation to the microscopic concept of Andreev bound states (ABSs) formed within the JJ.

Coherent Andreev reflections of quasiparticles at the graphene-superconductor interfaces lead to the formation of ABSs [37]. These quasiparticle states transfer Cooper pairs across the junction in form of counter propagating electron-hole pairs [38]. Due to the electron-hole symmetry, the ABSs come in pairs; one state has negative energy $E_n^- \leqslant 0$ and the other has positive energy $E_n^+ = -E_n^-$, where n denotes a specific transport channel. The spectral gap δE quantifies the minimal transition energy between states with negative and states with positive energies. Each occupied state carries current proportional to the derivative of its energy with respect to phase. The sum over the set of all channels defines the total supercurrent [39], which can be expressed as

$$I_s(\varphi) = \frac{2\pi}{\Phi_0} \sum_n f(E_n^\pm) \frac{\partial E_n^\pm}{\partial \varphi}, \tag{9}$$

where $f(E_n^\pm)$ is a functional describing the occupation probability of the nth ABS. In equilibrium the functional is given by the Fermi-Dirac distribution.

At zero temperature and in the absence of photons, all ABSs with negative energies are occupied [$f(E_n^-) = 1$], whereas all ABSs with positive energies are empty [$f(E_n^+) = 0$]. In this situation the system is in the ground state and the occupation of the ABS spectrum is constant. Therefore, the supercurrent I_s is free of any fluctuations. By virtue of the fluctuation-dissipation theorem [40], there is no dissipation and the effective junction shunt conductance assumes $G_s \rightarrow 0$.

When finite electronic temperatures T and/or the absorption of photons from the electromagnetic environment are

considered, the situation becomes different; thermal activation and/or microwave-induced transitions will drive the system out of the ground state. The excitation-relaxation dynamics give rise to fluctuations in the ABS population, and correspondingly, in the supercurrent as well. Consequently, there is dissipation and a finite shunt conductance G_s appears [8]. When the spectral gap closes ($\delta E \rightarrow 0$) already small temperatures T and small photon energies hf will trigger fluctuations. We note that the fluctuations are determined by the temperature, the photon absorption and emission rates and as well by the relaxation time τ_{rel} of a nonthermal distribution toward a thermal one, which we express in the following as the energy $\gamma = \hbar/(2\tau_{\mathrm{rel}})$. In conclusion, this means that in general, both the inductive and dissipative part of a JJ depend on the ABS spectrum and the population dynamics within this spectrum.

Inherent to wide junctions—like the graphene JJ investigated here—is that there are various possible transport channels leading to many ABSs and hence to a dense ABS spectrum [41]. The phase dependence of the ABS spectrum is determined by the geometry of the JJ and its material properties, i.e., the superconducting gap Δ in the leads and the inverse transport time in the normal region that relates to the Thouless energy E_T. In the ballistic transport limit $E_T = \hbar v_F / L$, where v_F is the Fermi velocity in the normal region and L is the junction length. In the diffusive limit $E_T = \hbar D / L^2$, where $D = v_F l_{\mathrm{mfp}}/2$ is the diffusion coefficient determined by the elastic scattering mean-free path l_{mfp}. An important characteristics of JJs is whether they are in the "short" or "long" junction limit. The former case is realized when $E_T \gg \Delta$, while the latter holds in the opposite limit. The condition for the short junction limit can also be expressed with the coherence length ξ, which needs to be longer than L. In the ballistic case the coherence length reads $\xi = \hbar v_F / \Delta$ and in the diffusive case $\xi = \sqrt{\hbar D / \Delta}$.

For JJs in the short junction limit the ABS energies are given by $E_n^\pm(\varphi) = \pm\Delta\sqrt{1 - \tau_n \sin^2(\varphi/2)}$, where τ_n is the transmission probability of the nth channel. Thus, the ABS spectrum strongly depends on the transparency distribution, which further defines the transport regime. For diffusive transport the transmission coefficients are continuously distributed following Dorokhov's bimodal distribution [43], which describes that there are many channels with low transmission ($\tau_n \rightarrow 0$), but also many with high transmission probabilities ($\tau_n \rightarrow 1$). Consequently, a dense ABS spectrum emerges as illustrated in Fig. 7(a) with a spectral gap $\delta E = 2\Delta|\cos(\varphi/2)|$ that closes ($\delta E \rightarrow 0$) toward the π-points and maximally opens ($\delta E = 2\Delta$) toward the 0-points. In long, diffusive junctions the spectral gap evolves as $\delta E \approx 2 \times 3 E_T |\cos(\varphi/2)|$ [13].

To evaluate the dynamics of an ABS spectrum and translate it to lumped element quantities, we make use of theoretical works that predict the phase-dependent linear microwave response in terms of the susceptance B_J and the shunt conductance G_s [3,4]. For the following theoretical analysis we consider a diffusive multichannel JJ in the short junction limit at finite temperature coupled to a photonic environment of energy hf. Note that in the experiment the photonic environment is provided by the driven microwave resonator. The justification of the above mentioned junction classification for
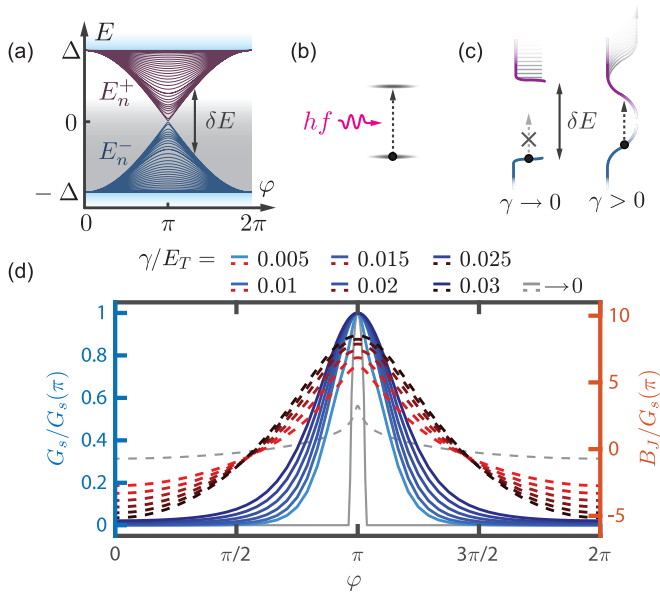
FIG. 7. ABS spectrum and theoretical microwave response for a short, diffusive JJ. (a) Spectrum of a short JJ with multiple channels of different transparencies. (b) Microwave-induced transitions between states triggered by the absorption of a photon with energy hf. (c) The finite lifetime of states described by the relaxation rate γ causes a spectral broadening of the ABS energies and hence blurs the transition condition. (d) Theoretically predicted dissipative and inductive response: G_s (blue, left axis) and B_J (red, right axis) normalized by the conductance value at $\varphi = \pi$ as a function of φ for different γ/E_T ratios. The normalization values for increasing γ/E_T read: $G_s(\pi)/G_N = 45, 11, 8.6, 7, 5.9, 5, 4.4$, where G_N is the normal state conductance. Here: $\Delta/E_T = 0.1$, $hf/E_T = 0.01$, and $kT/E_T = 0.008$.

the graphene JJ investigated here is discussed in the beginning of Sec. VIII.

We first focus on the dissipative response when long-lived excitations ($\gamma \to 0$) are considered. In this situation a sharp onset in $G_s(\varphi)$ emerges as seen by the solid gray line in Fig. 7(d). The dissipation occurs in the phase range, where the spectral gap becomes smaller than the excitation energy $\delta E \leqslant hf$, thus allowing microwave-induced cross-gap transitions. The width and the height of the dissipation peak depends on characteristic energy scales, which are denoted in the figure caption. Not only transitions across the gap lead to dissipation; all possible absorption processes, including intraband excitations $E_n^+ \to E_m^+$, contribute to it, whereas the transition probability scales according to Fermi′s Golden rule with the available density of states [13]. Figure 7(b) depicts a microwave-induced transition of a quasiparticle from an arbitrary initial state to an available final state. The fact that the ABSs have a finite lifetime causes a spectral broadening of the energies. This results in a blurring of the transition condition ($\delta E \leqslant hf$) as sketched in Fig. 7(c). Therefore, increasing γ, i.e., shortening the lifetime, broadens the dissipation peak as seen by the blue lines in Fig. 7(d). Importantly, the lifetime broadening also affects the susceptance, in particular the phase conditions for $B_J = 0$ shift away from the π-point, which is equivalent to a reduction of the CPR skewness. Note

that B_J for $\gamma \to 0$ shown in dashed gray appears different, because it is rescaled with a large conductance value $G_s(\pi)$. A representation of Fig. 7(d) without normalization is shown in the SM [23].

The influence of temperature on the microwave response is theoretically discussed, and together with experimental results, presented in the SM [23].

In short, environmental perturbations, namely, temperature and electromagnetic irradiation, cause dynamical variations in the population of ABS spectra on the timescale of the nonequilibrium occupation lifetime, which influence the susceptance B_J likewise the CPR and give rise to dissipation captured by the shunt conductance G_s.

VIII. COMPARISON WITH THEORY

Finally, we compare the experimental results of the graphene junction investigated here with theoretical predictions based on the assumption of a short, diffusive multichannel JJ. The condition for the short junction limit ($\xi > L$) seems reasonably valid, since the superconducting coherence length of similar devices is reported to be $\xi \approx 500$ nm [41,42] and the junction under investigation has a length $L = 400$ nm. The assumed predominant diffusive transport is supported by multiple observations: (i) the small discrepancy between the experimentally determined skewness at large n-doping ($S \approx 0.22$) and the one predicted theoretically ($S = 0.255$) [44], (ii) the lack of Fabry-Pérot oscillations in the gate dependence of the CPR presented in Fig. 5 indicates suppressed ballistic transport [29], and (iii) the randomly evolving shunt conductance G_s seen in Fig. 6 hints at universal conductance fluctuations, which are expected for diffusive systems. We believe that here the diffusive character of the device is stemming from scattering processes at the graphene edges, which are significant due to a small width to length ratio ($W/L \approx 2$), and hence reduce the amount of ballistic channels.

One theoretical prediction, which was not explicitly pointed out above, is that the inductive and dissipative response (B_J, G_s) scale linearly with the normal state conductance G_N [3,4], which is tunable with the gate voltage in our experiment. From Fig. 8(a) one can verify this relation, since the relation between the experimentally deduced values of the susceptance B_J and conductance G_s obtained at $\varphi = \pi$ for all different V_{bg}—clearly follows a linear trend. Furthermore, the ratio B_J/G_s is the inverse loss tangent describing the quality of the Josephson inductance [14], where a larger ratio implies a more ideal behavior of the inductance. We attribute the cone-shaped spread in Fig. 8(a) around the mean ratio ($\langle B_J(\pi)/G_s(\pi)\rangle \approx 7$) to altered ABS spectra and modified relaxation dynamics at different gate voltages.

In the next step, we search for the best match between the theoretically predicted and the experimentally deduced phase-dependent microwave response by considering both the inductive and the dissipative properties of the JJ. To this end, we numerically generate sets of B_J and G_s with different characteristic parameters. In particular, we vary the ratios kT/E_T and γ/E_T to account for a finite electronic temperature and to capture the effect of lifetime broadening. We have fixed the Thouless energy to $E_T = 10\Delta$ and the photon energy to $hf = \Delta/10$: the first condition ensures the short junction
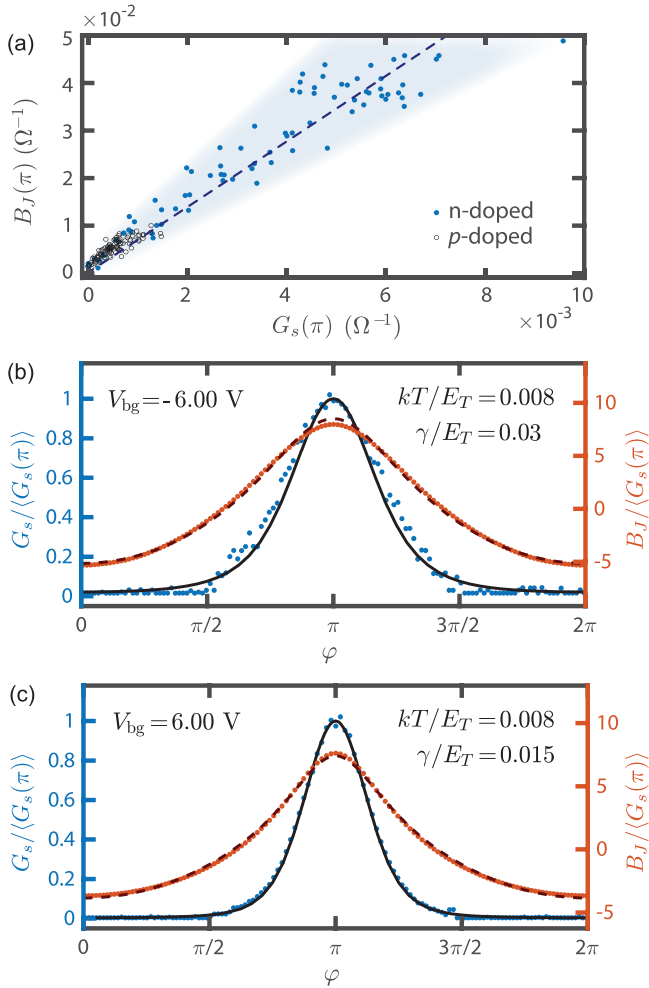
FIG. 8. Experimental observations in comparison with theoretical predictions for a short, diffusive JJ. (a) Experimentally obtained susceptance B_J versus shunt conductance G_s at $\varphi = \pi$ follows a mean ratio of ~ 7 indicated with the dashed line. (b, c) Normalized measured G_s (dotted blue, left axis) and B_J (dotted red, right axis) overlaid with the normalized theoretical predictions for G_s (solid) and B_J (dashed), for which $\Delta/E_T = 0.1$ and $hf/E_T = 0.01$ are fixed, but kT/E_T and γ/E_T are variable. The best fitting parameter ratios are indicated. For $V_{bg} = -6$ V (6 V) the normalizations read $\langle G_s(\pi)\rangle = 0.98\,\text{m}\Omega^{-1}$ ($5.19\,\text{m}\Omega^{-1}$) for the experimental traces and for the theoretical traces $G_s(\pi)/G_N = 4.4\,(7)$.

limit, whereas the second one compares favourably well to the expected experimental relation between the photon energy of the resonator and the superconducting gap of the contact material. Because in our experimental setting we are only sensitive to the low-energy ABS spectrum, the precise choice of E_T is irrelevant as long as the short junction limit can be assumed.

In Figs. 8(b) and 8(c) we compare the normalized theoretical and experimental values for $V_{bg} = -6$ V and $V_{bg} = 6$ V. The experimental values G_s (blue dots) and B_J (red dots) are normalized with the shunt conductance at $\varphi = \pi$, denoted by $\langle G_s(\pi)\rangle$ [45]. Close overlap between theory and experiment can be found for both gate voltages with the same temperature ($kT/E_T = 0.008$), but distinct relaxation rates γ.

At $V_{bg} = -6$ V we observe differences between the model and the experimental data even with the best match ($\gamma/E_T = 0.03$). This is especially evident at the flanks of the dissipation peak and the susceptance at the π-point. We attribute this mismatch to an inappropriate choice of transport regime for this gate voltage, because here the additional pn'-junctions at the interfaces effectively elongate the quasiparticle trajectories. Consequently, the JJ tends to be in the long-junction limit causing a compression of the ABS spectrum.

However, we stress that we observe striking agreements between the theoretical predictions with $\gamma/E_T = 0.015$ and the experimental data at $V_{bg} = 6$ V. Apparently, the model of a short, diffusive junction reproduces simultaneously the inductive and dissipative response of the graphene JJ for this doping configuration. By evaluating the best fitting ratios $kT/hf = 0.8$ and $\gamma/hf = 1.5$ with the resonance frequency $f = 3.098$ GHz, we deduce an electronic temperature $T = 120$ mK and obtain a relaxation time $\tau_{rel} = 17$ ps. A similar equilibration time ($\tau_{rel} = 7$ ps) is reported for an equivalent short, diffusive Al-graphene JJ probed at mK temperatures and large n-dopings [46]. We stress that the ABS spectrum of a short, diffusive junction might not be the only spectrum, which in a similar theoretical model could reproduce the experimentally observed response. In particular, in a wide JJ the ABS spectrum can be built from quasiparticles with long and short trajectories leading to more complex ABS structures than discussed here [41]. Therefore, the relaxation time given above should be interpreted as an order of magnitude estimation.

IX. CONCLUSION

We have measured the reflective response of a microwave resonator inductively coupled to a graphene-based rf SQUID as a function of flux-bias and charge carrier density. We developed a concise circuit model to infer the CPR and the phase-dependent dissipation of the graphene JJ from the changes in the resonance frequency and broadening. We hereby obtain the full complex admittance of the junction, which is the key parameter to design Josephson microwave circuits.

Our comprehensive investigation demonstrates the impact of the environment on the performance of JJs in terms of finite temperature and microwave photons. If the environment provides energies larger than the spectral gap, short-lived excitations appear in the ABS spectrum, which induce fluctuations in the supercurrent leading to dissipation. The comparison between the experimentally deduced microwave response at high electron density and the one predicted by theory for a short, diffusive junction model, yields striking agreement, from which we estimate a relaxation time on the order of ~ 10 ps. This fast thermal relaxation makes graphene-based JJs unique candidates for highly sensitive and fast bolo- and calorimeters [16,17,47].

Furthermore, the device architecture and measurement protocols presented in this work are well-suited to explore the fundamental properties of other JJs, such as junctions made of 2D/3D topological insulators or Dirac and Weyl semimetals [48]. Particularly, the topological nature of these JJs can be

probed, because it is predicted that they host ABS states that cross at the π-points but possess opposite parities, meaning that microwave-induced transitions across the gap are prohibited [49]. As a consequence, it is expected that the dissipative character of topological JJs is distinctly different from trivial ones [50–52].

All raw- and metadata in this publication are available in numerical form together with the processing codes at Ref. [54].

ACKNOWLEDGMENTS

[1] I. O. Kulik, Macroscopic quantization and the proximity effect in S-N-S junctions, Zh. Eksp. Teor. Fiz. **57**, 1745 (1969) [Sov. Phys. JETP **30**, 944 (1970)].

[2] A. A. Golubov, M. Y. Kupriyanov, and E. Il'ichev, The current-phase relation in Josephson junctions, Rev. Mod. Phys. **76**, 411 (2004).

[3] P. Virtanen, F. S. Bergeret, J. C. Cuevas, and T. T. Heikkilä, Linear ac response of diffusive SNS junctions, Phys. Rev. B **83**, 144514 (2011).

[4] F. Kos, S. E. Nigg, and L. I. Glazman, Frequency-dependent admittance of a short superconducting weak link, Phys. Rev. B **87**, 174521 (2013).

[5] P. F. Bagwell, Suppression of the Josephson current through a narrow, mesoscopic, semiconductor channel by a single impurity, Phys. Rev. B **46**, 12573 (1992).

[6] A. Paila, D. Gunnarsson, J. Sarkar, M. A. Sillanpää, and P. J. Hakonen, Current-phase relation and Josephson inductance in a superconducting Cooper-pair transistor, Phys. Rev. B **80**, 144520 (2009).

[7] D. Averin and H. T. Imam, Supercurrent Noise in Quantum Point Contacts, Phys. Rev. Lett. **76**, 3814 (1996).

[8] A. Martín-Rodero, A. Levy Yeyati, and F. J. García-Vidal, Thermal noise in superconducting quantum point contacts, Phys. Rev. B **53**, R8891(R) (1996).

[9] B. Dassonneville, A. Murani, M. Ferrier, S. Guéron, and H. Bouchiat, Coherence-enhanced phase-dependent dissipation in long SNS Josephson junctions: Revealing Andreev bound state dynamics, Phys. Rev. B **97**, 184505 (2018).

[10] F. Chiodi, M. Ferrier, K. Tikhonov, P. Virtanen, T. T. Heikkilä, M. Feigelman, S. Guéron, and H. Bouchiat, Probing the dynamics of Andreev states in a coherent Normal/Superconducting ring, Sci. Rep. **1**, 3 (2011).

[11] M. Ferrier, B. Dassonneville, S. Guéron, and H. Bouchiat, Phase-dependent Andreev spectrum in a diffusive SNS junction: Static and dynamic current response, Phys. Rev. B **88**, 174505 (2013).

[12] B. Dassonneville, M. Ferrier, S. Guéron, and H. Bouchiat, Dissipation and Supercurrent Fluctuations in a Diffusive Normal-Metal Superconductor Ring, Phys. Rev. Lett. **110**, 217001 (2013).

[13] Z. Dou, T. Wakamura, P. Virtanen, N.-J. Wu, R. Deblock, S. Autier-Laurent, K. Watanabe, T. Taniguchi, S. Guéron, H. Bouchiat, and M. Ferrier, Microwave photoassisted dissipation and supercurrent of a phase-biased graphene-superconductor ring, Phys. Rev. Res. **3**, L032009 (2021).

[14] R. E. Lake, J. Govenius, R. Kokkoniemi, K. Y. Tan, M. Partanen, P. Virtanen, and M. Möttönen, Microwave admittance of gold-palladium nanowires with proximity-induced superconductivity, Adv. Electron. Mater. **3**, 1600227 (2017).

[15] R. Aguado, A perspective on semiconductor-based superconducting qubits, Appl. Phys. Lett. **117**, 240501 (2020).

[16] G.-H. Lee, D. K. Efetov, W. Jung, L. Ranzani, E. D. Walsh, T. A. Ohki, T. Taniguchi, K. Watanabe, P. Kim, D. Englund, and K. C. Fong, Graphene-based Josephson junction microwave bolometer, Nature (London) **586**, 42 (2020).

[17] R. Kokkoniemi, J.-P. Girard, D. Hazra, A. Laitinen, J. Govenius, R. E. Lake, I. Sallinen, V. Vesterinen, M. Partanen, J. Y. Tan, K. W. Chan, K. Y. Tan, P. Hakonen, and M. Möttönen, Bolometer operating at the threshold for circuit quantum electrodynamics, Nature (London) **586**, 47 (2020).

[18] J. G. Kroll, W. Uilhoorn, K. L. van der Enden, D. de Jong, K. Watanabe, T. Taniguchi, S. Goswami, M. C. Cassidy, and L. P. Kouwenhoven, Magnetic field compatible circuit quantum electrodynamics with graphene Josephson junctions, Nat. Commun. **9**, 4615 (2018).

[19] J. I.-J. Wang, D. Rodan-Legrain, L. Bretheau, D. L. Campbell, B. Kannan, D. Kim, M. Kjaergaard, P. Krantz, G. O. Samach,

F. Yan, J. L. Yoder, K. Watanabe, T. Taniguchi, T. P. Orlando, S. Gustavsson, P. Jarillo-Herrero, and W. D. Oliver, Coherent control of a hybrid superconducting circuit made with graphene-based van der Waals heterostructures, Nat. Nanotechnol. **14**, 120 (2019).

[20] F. E. Schmidt, M. D. Jenkins, K. Watanabe, T. Taniguchi, and G. A. Steele, A ballistic graphene superconducting microwave circuit, Nat. Commun. **9**, 4069 (2018).

[21] F. E. Schmidt, M. D. Jenkins, K. Watanabe, T. Taniguchi, and G. A. Steele, Probing the current-phase relation of graphene josephson junctions using microwave measurements, arXiv:2007.09795.

[22] L. Wang, I. Meric, P. Y. Huang, Q. Gao, Y. Gao, H. Tran, T. Taniguchi, K. Watanabe, L. M. Campos, D. A. Muller, J. Guo, P. Kim, J. Hone, K. L. Shepard, and C. R. Dean, One-dimensional electrical contact to a two-dimensional material, Science **342**, 614 (2013).

[23] See Supplemental Material at http://link.aps.org/supplemental/10.1103/PhysRevResearch.4.013198 for details about the device fabrication (Sec. SI), measurement scheme and calibrations (Sec. SII, SIII, and SX), procedures for fitting the resonance curve (Sec. SIV), derivations and validity proof for the formulas relating the resonant behavior to the electrical properties of the JJ (Sec. SV– SVIII), iterative fitting routine to correct for screening (Sec. SIX), and theoretical as well as experimental results as a function of temperature (Sec. SXI).

[24] M. S. Khalil, M. J. A. Stoutimore, F. C. Wellstood, and K. D. Osborn, An analysis method for asymmetric resonator transmission applied to superconducting devices, J. Appl. Phys. **111**, 054510 (2012).

[25] M. Göppl, A. Fragner, M. Baur, R. Bianchetti, S. Filipp, J. M. Fink, P. J. Leek, G. Puebla, L. Steffen, and A. Wallraff, Coplanar waveguide resonators for circuit quantum electrodynamics, J. Appl. Phys. **104**, 113904 (2008).

[26] E. U. Manual (Sonnet Software, Liverpool, NY, 2005), p. 50.

[27] S. Gevorgian, Basic characteristics of two layered substrate coplanar waveguides, Electron. Lett. **30**, 1236 (1994).

[28] C. D. English, D. R. Hamilton, C. Chialvo, I. C. Moraru, N. Mason, and D. J. Van Harlingen, Observation of nonsinusoidal current-phase relation in graphene Josephson junctions, Phys. Rev. B **94**, 115435 (2016).

[29] G. Nanda, J. L. Aguilera-Servin, P. Rakyta, A. Kormányos, R. Kleiner, D. Koelle, K. Watanabe, T. Taniguchi, L. M. K. Vandersypen, and S. Goswami, Current-phase relation of ballistic graphene Josephson junctions, Nano Lett. **17**, 3396 (2017).

[30] D. I. Indolese, P. Karnatak, A. Kononov, R. Delagrange, R. Haller, L. Wang, P. Makk, K. Watanabe, T. Taniguchi, and C. Schönenberger, Compact SQUID realized in a double-layer graphene heterostructure, Nano Lett. **20**, 7129 (2020).

[31] D. A. Manjarrés, S. Gómez Páez, and W. J. Herrera, Skewness and critical current behavior in a graphene Josephson junction, Phys. Rev. B **101**, 064503 (2020).

[32] E. M. Spanton, M. Deng, S. VaitiekÄnas, P. Krogstrup, J. Nygård, C. M. Marcus, and K. A. Moler, Currentphase relations of few-mode InAs nanowire Josephson junctions, Nat. Phys. **13**, 1177 (2017).

[33] P. Jung, S. Butz, S. V. Shitov, and A. V. Ustinov, Low-loss tunable metamaterials using superconducting circuits with Josephson junctions, Appl. Phys. Lett. **102**, 062601 (2013).

[34] F. Nichele, E. Portolés, A. Fornieri, A. M. Whiticar, A. C. C. Drachmann, S. Gronin, T. Wang, G. C. Gardner, C. Thomas, A. T. Hatke, M. J. Manfra, and C. M. Marcus, Relating Andreev Bound States and Supercurrents in Hybrid Josephson Junctions, Phys. Rev. Lett. **124**, 226801 (2020).

[35] I. V. Borzenets, F. Amet, C. T. Ke, A. W. Draelos, M. T. Wei, A. Seredinski, K. Watanabe, T. Taniguchi, Y. Bomze, M. Yamamoto, S. Tarucha, and G. Finkelstein, Ballistic Graphene Josephson Junctions from the Short to the Long Junction Regimes, Phys. Rev. Lett. **117**, 237002 (2016).

[36] J. Xue, J. Sanchez-Yamagishi, D. Bulmash, P. Jacquod, A. Deshpande, K. Watanabe, T. Taniguchi, P. Jarillo-Herrero, and B. J. LeRoy, Scanning tunnelling microscopy and spectroscopy of ultra-flat graphene on hexagonal boron nitride, Nat. Mater. **10**, 282 (2011).

[37] A. F. Andreev, The thermal conductivity of the intermadiate state in superconductors, Sov. Phys. JETP **19**, 1228 (1964).

[38] J.-D. Pillet, C. H. L. Quay, P. Morfin, C. Bena, A. Levy Yeyati, and P. Joyez, Andreev bound states in supercurrent-carrying carbon nanotubes revealed, Nat. Phys. **6**, 965 (2010).

[39] C. W. J. Beenakker, Universal Limit of Critical-Current Fluctuations in Mesoscopic Josephson Junctions, Phys. Rev. Lett. **67**, 3836 (1991).

[40] J. G. Hoffman, The fluctuation dissipation theorem, Phys. Today **15**(1), 30 (1962).

[41] L. Bretheau, J. I.-J. Wang, R. Pisoni, K. Watanabe, T. Taniguchi, and P. Jarillo-Herrero, Tunnelling spectroscopy of Andreev states in graphene, Nat. Phys. **13**, 756 (2017).

[42] C. Li, S. Guéron, A. Chepelianskii, and H. Bouchiat, Full range of proximity effect probed with superconductor/graphene/superconductor junctions, Phys. Rev. B **94**, 115405 (2016).

[43] O. Dorokhov, On the coexistence of localized and extended electronic states in the metallic phase, Solid State Commun. **51**, 381 (1984).

[44] The CPR of a short, diffusive junction in equilibrium can be expressed analytically, from which one obtains a skewness $S = 0.255$ at $T = 0$ [4,53] as indicated by the pink mark in Fig. 5. The reduced skewness in the p-doped regime ($S \approx 0.12$) we assign to an overall suppression of the transmission probability due to the formation of pn'-junctions at the graphene-superconductor interfaces.

[45] We average the three shunt conductance values closest to $\varphi = \pi$ to accommodate for scattering of the data.

[46] J. Voutilainen, A. Fay, P. Häkkinen, J. K. Viljas, T. T. Heikkilä, and P. J. Hakonen, Energy relaxation in graphene and its measurement with supercurrent, Phys. Rev. B **84**, 045419 (2011).

[47] D. K. Efetov, R.-J. Shiue, Y. Gao, B. Skinner, E. D. Walsh, H. Choi, J. Zheng, C. Tan, G. Grosso, C. Peng, J. Hone, K. C. Fong, and D. Englund, Fast thermal relaxation in cavity-coupled graphene bolometers with a Johnson noise read-out, Nat. Nanotechnol. **13**, 797 (2018).

[48] A. Murani, B. Dassonneville, A. Kasumov, J. Basset, M. Ferrier, R. Deblock, S. Guéron, and H. Bouchiat, Microwave Signature of Topological Andreev Level Crossings in a Bismuth-Based Josephson Junction, Phys. Rev. Lett. **122**, 076802 (2019).

[49] Y. Peng, F. Pientka, E. Berg, Y. Oreg, and F. von Oppen, Signatures of topological Josephson junctions, Phys. Rev. B **94**, 085409 (2016).

[50] R. M. Lutchyn, J. D. Sau, and S. Das Sarma, Majorana Fermions and a Topological Phase Transition in Semiconductor-Superconductor Heterostructures, Phys. Rev. Lett. **105**, 077001 (2010).

[51] O. Dmytruk, M. Trif, and P. Simon, Josephson effect in topological superconducting rings coupled to a microwave cavity, Phys. Rev. B **94**, 115423 (2016).

[52] M. Trif, O. Dmytruk, H. Bouchiat, R. Aguado, and P. Simon, Dynamic current susceptibility as a probe of Majorana bound states in nanowire-based Josephson junctions, Phys. Rev. B **97**, 041415(R) (2018).

[53] T. T. Heikkilä, J. Särkkä, and F. K. Wilhelm, Supercurrent-carrying density of states in diffusive mesoscopic Josephson weak links, Phys. Rev. B **66**, 184513 (2002).

[54] R. Haller, Data and Code for "Phase-dependent microwave response of a graphene Josephson junction", Zenodo (2021), doi: 10.5281/zenodo.5996492.